Correlating Nanorod Structure with Experimentally Measured and Theoretically Predicted Surface Plasmon Resonance

Abrin L. Schmucker,[†,§] Nadine Harris,[†,§] Matthew J. Banholzer,[†,§] Martin G. Blaber,[†,§] Kyle D. Osberg,[‡,§] George C. Schatz,[†,§,*] and Chad A. Mirkin[†,‡,§,*]

[†]Department of Chemistry, [‡]Department of Materials Science and Engineering, and [§]International Institute for Nanotechnology, Northwestern University, 2145 Sheridan Road, Evanston, Illinois 60208-3113

ABSTRACT The extinction spectra of Au nanorods electrochemically synthesized using anodic aluminum oxide templates are reported. Homogeneous suspensions of nanorods with average diameters of 35, 55, 80, and 100 nm and varying lengths were synthesized, and their resultant surface plasmon resonances were probed by experimental and theoretical methods. Experimental extinction spectra of the nanoparticles exhibit good overall agreement with those calculated using the discrete dipole approximation. We determine the dependence of the dipole plasmon wavelength on both rod length *and* diameter, and we then utilize these results to derive an equation for predicting longitudinal dipole resonance wavelength for nanorod dimensions beyond the quasistatic limit. On average, the equation allows one to predict plasmon resonance maxima within 25 nm of the experimentally measured values. An analysis of factors that are important in determining the plasmon width is also provided. For long rods, the width decreases with increasing length in spite of increased radiative damping due to increased frequency dispersion in the real part of the metal dielectric function.

KEYWORDS: surface plasmon resonance · gold nanorods · nanoparticle · discrete dipole approximation · templated synthesis

Advances in methods for the synthesis of noble metal nanomaterials have given rise to increasingly sophisticated structures, including nanorods,[1−5] cubes,[6] triangular prisms,[7−10] triangular bipyramids,[11,12] cages,[13] and many others.[14−17] When these particles are irradiated with light, a coherent oscillation of conduction electrons known as a surface plasmon resonance (SPRs) can be induced at specific frequencies or wavelengths.[18] This plasmon excitation has been harnessed for a variety of powerful applications including the synthesis of anisotropic nanoparticles,[7,8,10,12,19] plasmonic rulers,[20] and biosensors.[21−24] Plasmonically active nanorods are of particular interest because they can be easily made *via* a variety of methods, including solution-phase syntheses,[2−5] template-based electrochemical deposition,[25−30] and lithography-based techniques.[31,32] These synthetic capabilities allow one to prepare structures which often have SPRs that can be tuned from the visible to the near IR, depending upon structure dimensions.[5] Consequently, these structures have led to a variety of novel sensing,[20,33,34] imaging,[35] and therapeutic[35] platforms.

With these advances in the synthesis and characterization of noble metal nanorods, a number of groups, including ours, have been able to carry out a variety of structure−function correlations.[1,36−41] Extensive studies have been performed examining the effect of nanorod length and subsequently aspect ratio on SPR.[41−44] Novo *et al.* examined the optical properties of Au rods with aspect ratio between 2 and 4 with diameters between 8 and 30 nm.[45] However, to date, no exhaustive study has been performed exploring a broad range of nanorod diameters examining its effect on the resulting SPRs. This is surprising since understanding the relationship between structural parameters and plasmonic effects would allow for more rationally designed functional systems. Previous work has shown that increasing the aspect ratio of noble metal nanorods blue shifts transverse SPRs,[46] while red shifting longitudinal dipole[1,35] and multipole[36] SPRs. This shifting of plasmon resonances was first described in 1912 by Gans[47] when he provided an analytical solution for the depolarization factor for spheroids of arbitrary aspect ratio (see Supporting Information for a discussion of Gans theory). Additional work has studied the relationship between nanorod diameter and longitudinal dipole SPR to develop an equation to
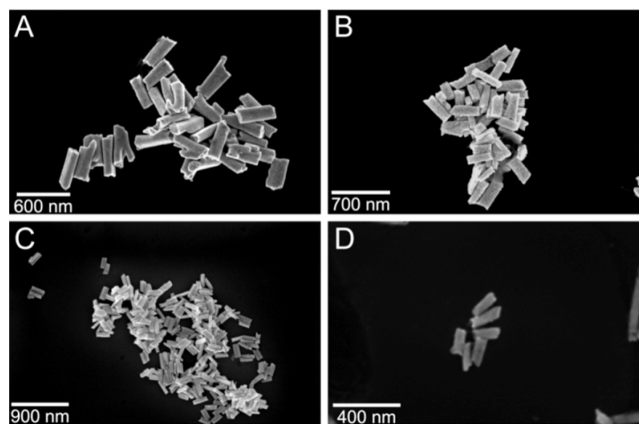
Figure 1. Scanning electron microscopy images of Au wires of similar aspect ratios and varying diameter: (A) 100 nm (aspect ratio 4.0 ± 0.4), (B) 80 nm (aspect ratio 4.0 ± 0.5), (C) 55 nm (aspect ratio 3.3 ± 0.4), and (D) 35 nm (aspect ratio 4.3 ± 0.6).

predict the SPR wavelength.[48] While this preliminary study has begun to explore the effects of nanoparticle diameter on the longitudinal dipole SPR in the small diameter range, additional effects appear as diameter is increased because in this range there are radiative effects which make the SPR wavelength strongly dependent on diameter.[45,49,50] These effects are especially critical in many sensing applications where the larger diameter nanorods that are fabricated using electrochemical methods are useful for index of refraction and SERS measurements. Indeed, a thorough understanding of how these modes vary with structure is therefore necessary in order to fully utilize these systems. Additionally, since many applications often require SPR bands at specific locations in the spectrum, a predictive analytical equation to determine SPR wavelength is desirable.

Nanorods synthesized using template-based electrochemical syntheses are ideal for studying the influence of structural parameters on SPR. This approach allows one to finely adjust nanowire dimension with precise control over length, diameter, and composition.[37,51−53] Having length control that is independent of diameter is a distinct advantage over solution-phase synthesized rods. The spectroscopy of these wires, combined with discrete dipole approximation (DDA) calculations, allows one to identify significant trends and to develop design rules for the optical properties of the Au nanorods. These *a posteriori* rules allow one to accurately produce nanowires with a specific set of optical properties, eliminating the need for lengthy characterization and optimization cycles to achieve the desired properties. Herein, we report a comprehensive examination of the interplay between diameter and aspect ratio on the longitudinal dipole SPR of Au nanorods for a multitude of particle dimensions. This research has allowed us to expand upon previously reported results[40,48] to include radiative damping effects, which ultimately leads to a more accurate predictive

model for SPR position. We also use the results to study the variation of plasmon width with rod structure, demonstrating that longer rods have narrower resonances for all diameters.

RESULTS AND DISCUSSION

Au rods were synthesized electrochemically with varying lengths and diameters using a template-based approach.[25,28,46] Anodic aluminum oxide (AAO) serves as the template for synthesis and can be fabricated in house following the protocol developed by Masuda and co-workers[54] or purchased directly from Synkera Technologies Inc. in a variety of pore widths. Because pore diameter and electric charge passed during synthesis control the resulting nanorod diameter and length,[27] respectively, we were able to produce wires with aspect ratios of approximately 8:1, 6:1, 4:1, 2:1, and 1:1 for rods with diameters of 100, 80, 55, and 35 nm, respectively, and having an average size distribution of $\bar{x} = 14\%$ (Figure 1, Figure S1 and Table S1, Supporting Information).

To correlate particle architecture with optical properties (*i.e.*, SPR location), extinction measurements were carried out on all of the synthesized rods (Figure 2A-D; see also Table S1, Supporting Information, for SPR λ_{max}). The maximum extinction value for each spectrum has been normalized to 1 for comparison and clarity purposes. This is important since charge separation along the rod increases with increasing aspect ratio, causing the magnitude of the dipole extinction to increase and consequently dwarf the higher order resonance modes.[48] In agreement with previous work,[36,47] the transverse and longitudinal dipole SPRs overlap in particles with aspect ratios ≈1 due to their isotropic nature. With increasing aspect ratio, these resonances separate due to changes in depolarization, and the longitudinal dipole begins to red shift from visible to infrared wavelengths. For example, 35 nm diameter rods with an aspect ratio of 1.2 have a resonance at 581 nm. Changing the aspect ratio of the rods to 4.3 by increasing their length shifts the dipole resonance to 1034 nm. A further increase in aspect ratio to 6.9 shifts the resonance to 1401 nm. Similar trends in the red shift of the longitudinal dipole SPR can be seen with rods of larger diameters. This effect can be understood by utilizing Gans theory, where the SPRs of spheroids were shown to vary in magnitude and position by simply varying the aspect ratio of the spheroids or the dielectric constant of the surrounding medium (eq S4, Supporting Information).[47]

The magnitude of this red shift makes the interrogation of SPR location problematic for rods of larger diameters and aspect ratios because the longitudinal dipole resonance cannot be measured experimentally due to solvent limitations (D_2O absorbs at $\lambda > 1800$ nm). Of course, this is not a limitation for the DDA calculations, so we have used DDA to help assign and characterize
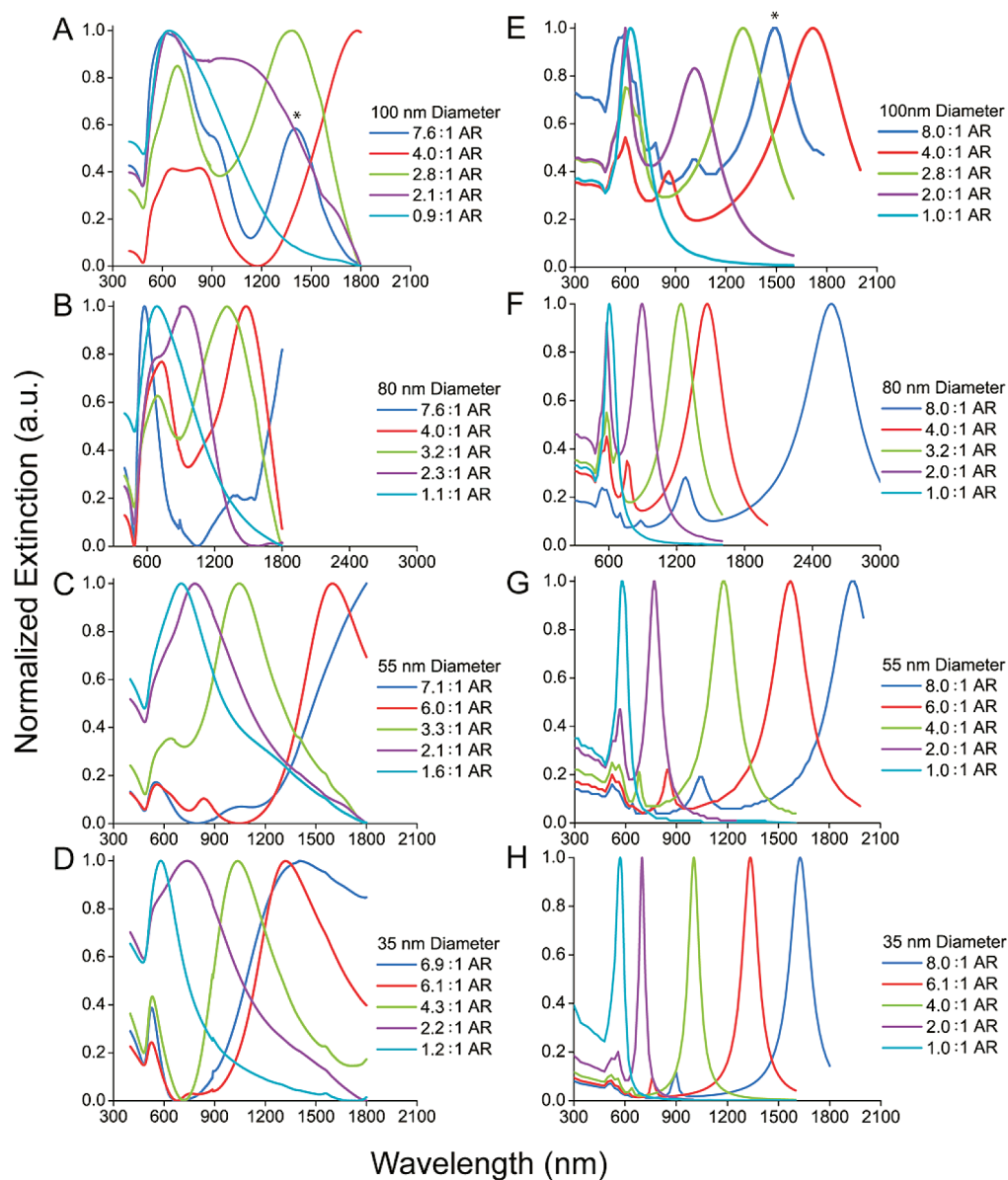
Figure 2. Normalized extinction spectra for electrochemically synthesized Au wires in D_2O having (A) 100 nm, (B) 80 nm, (C) 55 nm, and (D) 35 nm diameters. Normalized extinction spectra for orientation-averaged Au nanorods of (E) 100 nm, (F) 80 nm, (G) 55 nm, and (H) 35 nm diameters as modeled by the discrete dipole approximation (DDA). Different traces on graphs indicate rods of different aspect ratio, as specified by their individual legends. Asterisks in panels A and E denote the prominent quadrupole resonance mode of these structures. The dipole resonance was not observable within the range of wavelengths tested.

the spectra. In this method, the nanorod is represented as a cubic array of elements where the polarizability α_i of each element is calculated based upon the dipole dielectric properties and position within the target r_i.[55−57] Dielectric constants used for these calculations are from Frederikse and Weaver.[58] The spectra of orientation-averaged wires modeled by DDA calculations display trends similar to those synthesized electrochemically (Figure 2E−H). Note also that all even and odd higher order modes are present in the extinction spectra because the induced polarization is not necessarily symmetrical with respect to the rod axis.[36] This is in contrast to what happens for fixed orientation, where certain even multipoles are symmetry forbidden. The

DDA calculated extinction spectra also show that increasing the aspect ratio and diameter red shifts the dipole plasmon resonance in addition to slightly blue shifting the transverse dipole resonance. This familiar red shifting of the dipole resonance phenomenon has been measured and calculated in the past[36,59] and demonstrates the extraordinary tunability of SPR for Au nanorods.

The DDA method is capable of modeling particles not considered in the quasistatic (Gans) regime, allowing the calculation of higher order modes and the inclusion of radiative effects. This allows us to more directly compare experimental results to predicted values. Figure 2H shows that higher order modes are apparent for
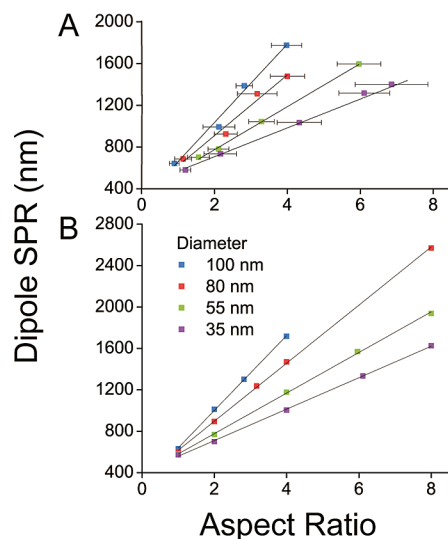
Figure 3. Longitudinal dipole SPR as a function of aspect ratio for (A) wires synthesized electrochemically for 100, 80, 55, and 35 nm diameters in solution. (B) Orientation-averaged wires modeled by DDA for rods of the same diameter as the experimental samples.

the 35 nm diameter particles with aspect ratios greater than 4 where the dipole resonance is present at 1004 nm and the $l = 2$ higher order mode at 636 nm. As the aspect ratio of this rod increases, an additional resonance, $l = 3$, becomes evident for the 6.11 aspect ratio rod. In this case, the dipole resonance is at 1334 nm, $l = 2$ at 764 nm, and $l = 3$ at 620 nm, where l is the multipole order. The DDA-based extinction spectra are also in agreement with Khlebstov *et al.*,[60] who used the T-matrix method to model Au cylinders. In that work, among other things, it was shown that the absorption and scattering positions of the multipoles are the same, and for the smaller diameter rods, the multipolar resonances are dominated by absorption and larger diameter rods are dominated by scattering.

To better elucidate trends in the bulk data shown in Figure 2, we examined plots of the longitudinal dipole SPR as a function of aspect ratio for a variety of rods (Figure 3). In both the experimental results and those modeled by DDA, the dipole SPR position increases linearly with increasing aspect ratio having a

correlation coefficient (R^2) ≥ 0.961 and ≥0.999, respectively. However, there is also a strong dependence on nanoparticle diameter for a given aspect ratio. Combining both aspect ratio and diameter data allows us to construct a two-dimensional graph for the longitudinal dipole resonance as a function of aspect ratio *and* diameter (Figure 4). From these data, it is clear that both parameters (aspect ratio and diameter) have a significant influence on SPR position and can be used independent of each other to adjust the SPR positions as desired. Utilizing this plot can provide an approximation for longitudinal dipole SPR wavelength for rods of any diameter and aspect ratio, within the range tested, to be used as a guide to adjust the parameters of the electrochemical synthesis to produce rods having SPRs of desired wavelength.

The often reported linear relationship between the wavelength position of the SPR and the aspect ratio is dependent on the free electron character of the metal. For metals with low Drude scattering rates, γ, which includes electron−electron, electron−phonon, and impurity scattering, the SPR red shift is almost linearly dependent on aspect ratio. The rate of red shift with increasing aspect ratio is inversely proportional to the plasmon frequency, ω_p. High plasmon frequencies reduce the rate of red shift because the real part of the dielectric constant decreases more rapidly with increasing wavelength. For a Drude metal (with frequencies in eV), the resonant wavelength for a prolate spheroid in the quasistatic limit is given by (see Supporting Information for details)[18,47]

$$\lambda_p = \beta / \sqrt{\frac{L_1 \omega_p^2}{\varepsilon_m + L_1(1 - \varepsilon_m)} - \gamma^2} \qquad (1)$$

where β is a constant (1239.85 nm eV), ε_m the dielectric constant of the medium, L_1 is the depolarization factor related to aspect ratio such that

$$L_1 = \frac{1 - e^2}{e^2}\left(-1 + \frac{1}{2e}\ln\frac{1 + e}{1 - e}\right) \qquad (2)$$

where e is the eccentricity of the ellipse, which is described by $e^2 = 1 - (b/a)^2$; a and b are the radii of the
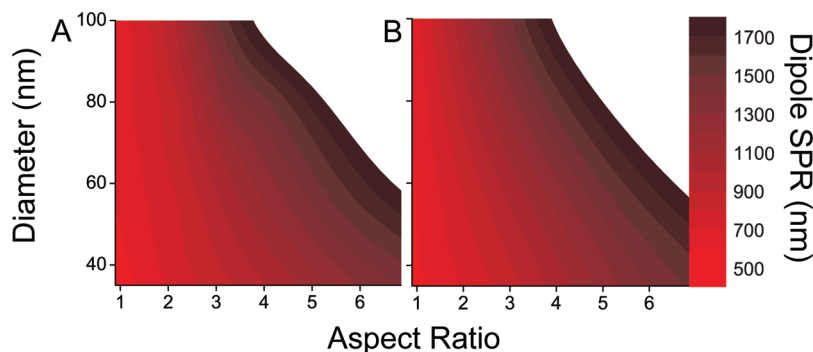

Figure 4. Contour plot of the longitudinal dipole SPR wavelength for Au nanorods as a function of diameter and aspect ratio. (A) Experimental values of longitudinal dipole SPR as a function of both aspect ratio and diameter. (B) Corresponding DDA results.

spheroid along the semilong and semishort axes, respectively. It is evident from eqs 1 and 2 that the relationship between SPR position and aspect ratio is nontrivial in general. However, in the limit of small b/a (but not too small) and small widths γ, eq 1 reduces to $\lambda_p = (\beta/\omega_p)\sqrt{\varepsilon_m(a/b)} \times$ (slowly varying function of a/b), which is linear in aspect ratio, with the expected inverse dependence on ω_p. Going back to eq 1, if we plot λ_p for Drude metals with varying plasmon frequencies and Drude scattering rates (Figure S2, Supporting Information), the relationship between λ_p and aspect ratio is found to be essentially linear.

Upon examination of the data set, it is apparent that the diameter dependence is not as simple as the aspect ratio dependence. It is common practice to graph the wavelength of the resonance as a function of aspect ratio for varying rod diameters because, originally, this was applied to rods in the quasistatic limit. However, it has been shown[50,61] that the quasistatic criteria are very stringent and do not apply to any of the rods that we have considered. If these criteria did apply, the SPR, normalized to the peak extinction value, would be dependent upon the aspect ratio only and spectra for rods of differing diameter would be superimposable. Because the SPR has a strong dependence on nanorod diameter, it is clear that the quasistatic limit does not apply.

To study the dependence of plasmon wavelength on diameter, we have generated regression plots of the longitudinal dipole resonance for the experimentally determined and DDA calculated SPRs as a function of diameter for a variety of aspect ratios (Figure 5). Data for Figure 5A were calculated using equations derived from linear regressions in Figure 3 to compare experimental and theoretical results for rods having identical aspect ratios. This shows that the relationship between dipole resonance and rod diameter is nonlinear. A second-order polynomial fit has been applied to each of the curves with R^2 values for the experimentally calculated and DDA calculated values of ≥ 0.946 and ≥ 0.999, respectively. The dipole plasmon resonance for very small particles approaches the quasistatic limit, so the curves approach a horizontal straight line as the diameter of the particle becomes small. As the diameter of the particle increases, the influence of radiative damping becomes evident and the curves become nonlinear. This effect was also observed for the quadrupole resonance of the nanorods. While a linear relationship exists between quadrupole resonance and aspect ratio, as seen previously,[36] a nonlinear relationship exists between this resonance and diameter (Figure 6). The absence of these resonances in the lower aspect ratio rods prevented the addition of these data points within these figures. Nevertheless, the nonlinear trend is evident.

To fully describe this system with a predictive analytical model, we must add an additional correction
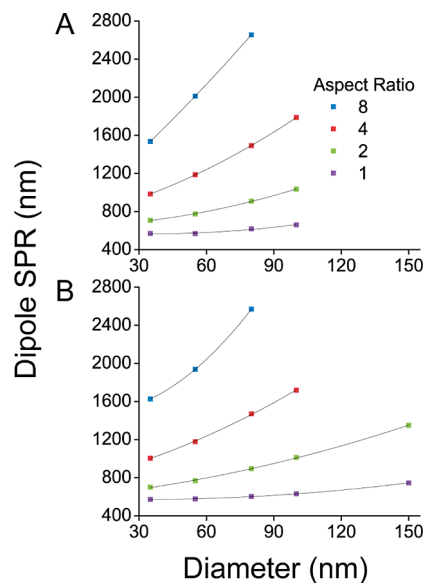

Figure 5. Longitudinal dipole SPR as a function of diameter. (A) Values for the experimental longitudinal dipole SPR calculated from linear regressions applied in Figure 4. Values were fit to a second-order polynomial having a minimum R^2 value of 0.95. (B) DDA results of dipole SPR; 150 nm diameter rods of 2-1 and 1-1 aspect ratio were modeled to further confirm the nonlinear result. All fits have a minimum R^2 value of 0.998.

term to Gans' theoretical description of the quasistatic spheroid to compensate for the radiative damping effects. This derivation follows a similar vein to that described by Meier and Wokaun,[62] who developed finite size corrections for a sphere by examining the induced dipole moment of the sphere due to the applied electric field.[63]
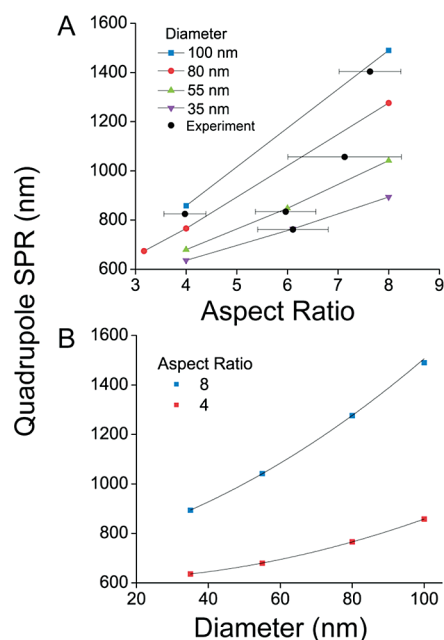

Figure 6. Quadrupole plasmon resonance as a function of (A) aspect ratio for different diameters and (B) diameter for the two aspect ratios having $l = 2$ quadrupole resonances.

In the quasistatic regime, the induced dipole moment of a spheroid is given by[18]

$$\mathbf{P} = \alpha\mathbf{E} \tag{3}$$

where $\mathbf{E}$ is the incident electromagnetic field and the polarizability of a spheroid is given by[64]

$$\alpha_x = 4\pi abc \frac{\varepsilon_1 - \varepsilon_m}{3\varepsilon_m + 3L(\varepsilon_1 - \varepsilon_m)} \tag{4}$$

where a is the length of the longitudinal (or major semiaxis) axis and b is the shorter semiaxes; ε_1 and ε_m are the dielectric functions of the spheroid and surrounding medium, respectively, and L is the geometrically dependent depolarization factor (eq 2).

To correct for radiative damping, the radiation correction field, $\mathbf{E}_{rad}$, must first be calculated and then included in eq 3 such that[18]

$$\mathbf{P} = \alpha[\mathbf{E} + \mathbf{E}_{rad}] \tag{5}$$

Moroz[65] has recently developed a rigorous solution to the radiative damping term for a spheroid. The result given by Moroz is similar to eq 6, which was developed in a slightly less rigorous manner by Zemen et al.[63] Nevertheless, eq 6 shows good agreement with full electromagnetic spheroidal calculations.[18]

$$\mathbf{E}_{rad} = \frac{2}{3}ik^3\mathbf{P} + \frac{k^2}{a}\mathbf{P} \tag{6}$$

Finally, calculation of the size-corrected induced dipole moment involves multiplying eq 3 by[18]

$$G = \frac{1}{\left(1 - \frac{2}{3}ik^3\alpha - \frac{k^2}{a}\alpha\right)} \tag{7}$$

The first term in the denominator of eq 7, $2/3ik^3\alpha$, is the radiative damping contribution to the damping of the dipole resonance and is a function of spheroid volume.[65] The second term, $(k^2/a)\alpha$, is a depolarization contribution which depends on spheroid area. For nearly spherical particles, the $(k^2/a)\alpha$ term produces strong red shifts as spheroid size increases, while for more prolate spheroids, this term increases the red shifting with increased aspect ratio beyond what comes from the quasistatic approximation. This red shifting can be seen in Figure 7A, where DDA, modified long wavelength approximation (MLWA), and quasistatic methods were used to calculate the dipole resonances for 80 nm diameter rods with increasing aspect ratio. The difference between the quasistatic and MLWA dipole resonance peak positions is due to the depolarization term, while the difference between the MLWA and the DDA results is caused by shape effects (rod versus spheroid). In addition, plotting the dipole resonance wavelength as a function of diameter shows the nonlinear relationship between rod diameter and dipole resonance for the MLWA and DDA results due to depolarization (Figure
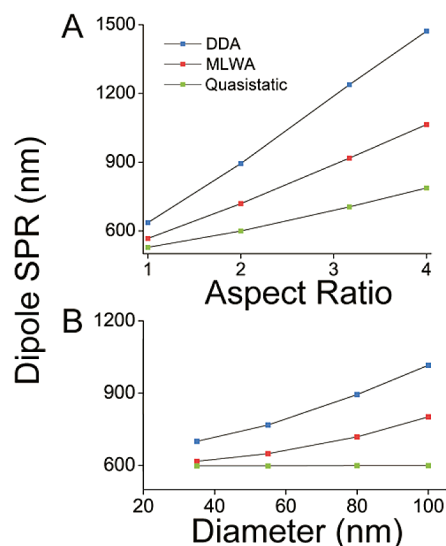

Figure 7. Dipole SPR position for Au nanorods of (A) 80 nm diameter with changing aspect ratio calculated by DDA, MLWA, and quasistatic theory and of (B) aspect ratio 2 with varying rod diameter.

7B). The dipole resonance wavelength in this figure remains constant for the quasistatic results because only aspect ratio appears in eqs 1 and 2.

Encina and Coronado[48] developed a model, applicable to cylindrical rods with fixed orientation, that enables one to calculate the resonance wavelength of any mode for a rod of any size and any noble metal. The model is described by finding the value of the dielectric function which satisfies the relation

$$\varepsilon(\lambda_{res}) = -f\varepsilon_m \tag{8}$$

where λ_{res} is the resonant wavelength and f is equivalent to the previously discussed geometry-dependent depolarization factor. A very comprehensive set of calculations was performed on rods, in vacuum, with diameters between 8 and 50 nm and lengths of 80 to 1600 nm. Linear regression analysis was used to determine the constants A (2687 μm^{-2}), B (4.4), and C (3.7) in the following equation:

$$\text{Re}[\varepsilon(\lambda_{res})] = -f\varepsilon_m = -\left(\frac{A}{Q^2} + \frac{B}{Q^2 d^2} + C\right)\varepsilon_m \tag{9}$$

where $Q = l\pi/L$, L is the rod length, l is the resonance mode of interest, and d is the diameter.

Recently, Slaughter et al.[40] reported the use of this model to compare directly with their measured single particle spectra and found good agreement. We applied this model to our structures but observed large discrepancies when compared to our own results (Figure S4, Supporting Information). To investigate the cause, additional calculations were run utilizing their source of dielectric data,[66] rather than ours,[58] for consistency (Table S4, Supporting Information). Because we observed minimal change, we can conclude that the discrepancy lies in the depolarization contribution seen in the

larger diameter rods considered here. Following their protocol for generating a predictive model,[48] we determined that, within the range of rods geometries synthesized, the longitudinal dipole SPR could be better described by

$$\lambda_{res} = I\left(-\frac{\alpha}{10^4 Q^4} + \frac{\beta}{10^4 Q^2} + \gamma\right)^2 - J\left(-\frac{\alpha}{10^4 Q^4} + \frac{\beta}{10^4 Q^2} + \gamma\right) + K \quad (10)$$

where α and β are functions of diameter, and γ, I, J, and K are constants (see Supporting Information for a full description of model derivation).

Now let us consider the plasmon width. This property provides useful insight into the effect of radiative damping on particle spectra. Unfortunately, the elucidation of width values from the experimental data is problematic due to size dispersion and absorbing background media. We therefore perform our analysis using DDA, MLWA, and quasistatic results. In the following, we define the width by evaluating the full width at half-maximum (fwhm) for spectra plotted as a function of photon energy (rather than wavelength). This width is plotted *versus* nanorod length in Figure 8, and it is immediately apparent that, for all theoretical results, the width decreases with rod length (at least in the limit of long enough rods). This is in contrast to the wavelength-based peak widths in Figure 2 which show the opposite behavior. We will only consider energy-based widths in the following discussion.

The DDA, MLWA, and quasistatic results in Figure 8 show the same trends, but the DDA fwhm is generally larger than MLWA, and MLWA is always larger than quasistatic. Of course, the comparison of MLWA and quasistatic is easily understood, as the MLWA results include for radiative damping while quasistatic does not. The comparison of DDA and MLWA widths involves two issues. First, the particle geometries are different, and there are likely intrinsic differences in widths that arise because of the sharp corners in the cylinders compared to the smooth surfaces of the spheroids. Second, the SPR peaks of the DDA calculations are considerably more red-shifted than the MLWA (due to particle shape issues) (Table S5, Supporting Information), which necessarily reduces their line width due to frequency dispersion effects that we now discuss.

Of note is the decrease in the SPR fwhm with increasing length for all theories, indicating that the increase in width due to radiative damping is less important in the large particle limit than the increased dispersion in the real part of the dielectric constant (*i.e.*, increase in the magnitude of the slope of the dielectric function) as wavelength increases. To elaborate, in the quasistatic limit, the condition for resonance can be determined by setting the denominator of eq 4 to 0. As the depolarization factor is a real quantity *via* the
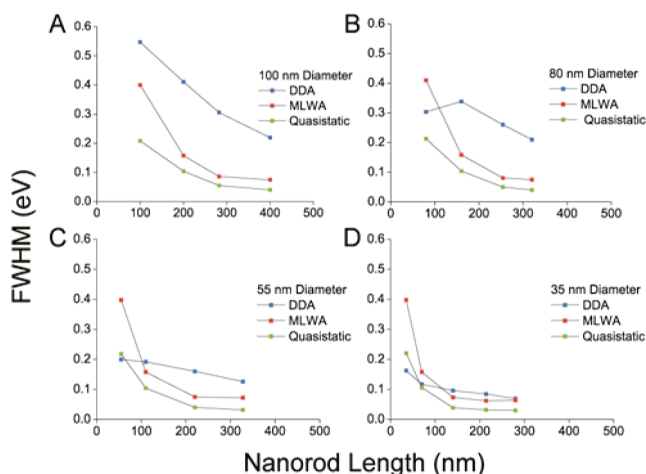

Figure 8. Full width at half-maximum values as a function of rod length for DDA, MLWA, and quasistatic calculations for rod and spheroid diameters of (A) 100 nm, (B) 80 nm, (C) 55 nm, and (D) 35 nm.

definition (eq 2), we let $\varepsilon'' \to 0$. The solution becomes $L = \varepsilon_m/(\varepsilon_m - \varepsilon'_1)$. Substituting this into eq 4 and selecting the imaginary part gives the polarizability at resonance.[67]

$$\alpha_p \approx iV\frac{(\varepsilon_m - \varepsilon'^2_1)}{\varepsilon_m \varepsilon''_1} \quad (11)$$

The fwhm of the SPR is related to the derivative of the real part of the dielectric constant with respect to frequency. Increasing the aspect ratio of the rod (and hence the depolarization factor) decreases the resonant dielectric constant, making it more negative. As the dielectric constant is decreased, its derivative with respect to frequency, $d\varepsilon'_1/d\omega$, increases, narrowing the fwhm of the SPR. In the quasistatic limit, the fwhm, Γ_ω, at the resonant frequency ω is related to the derivative of the real part of the dielectric function:[68]

$$\Gamma_\omega \approx \frac{2\varepsilon''_1}{d\varepsilon'_1/d\omega} \quad (12)$$

For a Drude metal the derivative of the real part of the dielectric function is

$$\frac{d\varepsilon'_1}{d\omega} = \frac{2\omega\omega_p^2}{(\gamma^2 + \omega^2)^2} \quad (13)$$

This results in a fwhm which for $\omega \gg \gamma$ that is relatively independent of wavelength:

$$\Gamma_\omega^{Drude} = \frac{\gamma(\gamma^2 + \omega^2)}{\omega^2} \quad (14)$$

Interband transitions in Au cause the idealized fwhm from eq 12 (based on experimental data rather than Drude dielectric constants) to drop rapidly from 0.35 eV at 500 nm to 0.05 eV at 700 nm, plateauing at 0.03 eV for wavelengths above 800 nm. The DDA fwhm (Figure 8) slowly narrows for very large particles, indicat-
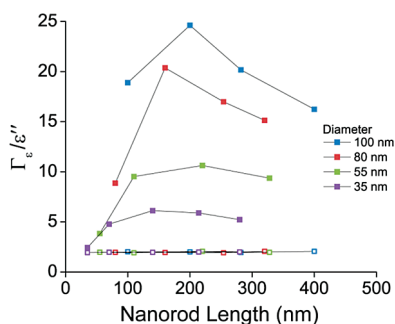
Figure 9. Line width written in terms of the real part of the dielectric function across the fwhm *vs* nanorod length. The line width is scaled by the imaginary part of the dielectric function at the resonance frequency. This provides a general measure of the amount of radiative damping. Results modeled by DDA are shown as solid symbols, while the quasistatic results are shown as hollow symbols. The quasistatic results do not include radiative effects, leading to horizontal lines.

ing that radiative damping due to finite size increases less rapidly than the shift in SPR due to increased length. Indeed, radiative effects increase with increasing size parameter (a/λ_p), relaxing the resonance condition and hence allowing for SPR over a broader range of frequencies. The change in the real part of the dielectric function across the fwhm, $\Gamma_\varepsilon = \varepsilon'(\omega + \Gamma_\omega/2) - \varepsilon'(\omega - \Gamma_\omega/2)$, is plotted as a function of length for both the DDA and quasistatic results (Figure 9). In order to remove nonradiative effects, the data in the plot are scaled by the value of the imaginary dielectric function on resonance. Two competing features are evident in this figure; the first is that additional size increases the size parameter, increasing radiative damping and Γ_ε (which increases the fwhm). The second is the red shift associated with increasing aspect ratio; this causes a narrowing of the resonance as larger dielectric function gradients (greater frequency dispersion) are accessed.

For the case of the 80 and 100 nm rods, radiative damping makes a substantial contribution to the line width; in the 2:1 aspect ratio case, the increased length (and hence size parameter) causes increased radiative damping, and the associated red shift is not sufficient to push the resonance to a region where $d\varepsilon'_1/d\omega$ is large, resulting in an overall increase in Γ_ε. As the aspect ratio is increased to 3:1, additional red shift begins to compensate for finite size effects and the Γ_ε narrows. For the 35 nm diameter wires, increases in aspect ratio leave Γ_ε almost constant, indicating that an equilibrium has been reached between radiative damping and resonance shift.

CONCLUSION

In conclusion, we have observed the effects of both aspect ratio and diameter on the transverse dipole SPR for a multitude of particle dimensions. We determined the interplay between aspect ratio and diameter on the optical properties of template-synthesized Au nanorods and show that the longitudinal dipole SPR is first order with respect to aspect ratio and second order with respect to diameter; these results have been corroborated by nanorods modeled by DDA calculations. Importantly, with this understanding of the relevant parameters that affect the optical properties of these structures, such as radiative damping, we are able to establish a set of experimental design rules for the dipole SPR position with good agreement with the DDA results. These rules could provide valuable insight when creating designer nanoparticles with resonances in specific and desired locations. Although inhomogeneous broadening made it impossible to use the experimental results to analyze plasmon widths, the theoretical results indicate that longer rods gradually reduce the plasmon width as rod length is increased. In this limit, frequency dispersion effects overcome increased radiative broadening for these structures.

EXPERIMENTAL DETAILS

In a typical experiment, 200 nm of Ag is thermally evaporated onto one side of the AAO template. The template is then placed in contact with an aluminum foil working electrode inside a Teflon electrochemical cell having a Pt counter electrode and Ag/AgCl reference electrode.[69] Next, the template is washed for several minutes to fully wet the interior of the pores. A sacrificial segment of Ag and is then initially deposited within the pores utilizing a Ag plating solution (Technic Silver Cy-less II) at a constant potential of -0.94 V. Following uniform deposition, the Au segments of interest are deposited using a Au plating solution (Orotemp-24 Rack RTU, Technic Inc.) at a constant potential of -0.94 V. The rod length was controlled by managing the amount of charge passed during the deposition. Deposition of sacrificial Ni segments (Nickel sulfamate RTU) at -0.91 V between multiple Au segments of interest were done to increase the absolute yield of the synthesis. Rods are then recovered by etching the Ag backing with a 4:1:1 mixture[70] of methanol, 30% H_2O_2, and 28% NH_4OH and dissolving the AAO template in 3 M NaOH. The sacrificial Ni segments are removed using HNO_3 (33% v/v), and the sample is subsequently mixed with a solution of

O-(2-carboxyethyl)-O'-(2-mercaptoethyl)heptaethylene glycol (Aldrich) (0.02% (v/v) in 10% EtOH (v/v)) for 1 h to stabilize the resulting Au rods and improve dispersion in solution. After rinsing three times with water and two times with EtOH, the rods are resuspended in D_2O *via* sonication. Scanning electron microscopy (SEM) images for determining particle morphology were taken on a Leo 1525. Experimental extinction spectra were collected on a Varian Cary 5000 UV−vis−NIR spectrophotometer and did not use polarized light. Experimental samples were measured from 400 to 1800 nm.

The discrete dipole approximation (DDA) was used to model the cylindrical-shaped Au nanorods in water. DDA was first developed in 1973 by Purcell and Pennypacker[57] as a numerical technique to calculate the absorption and scattering of electromagnetic radiation from arbitrary shaped targets. This technique was later developed by Draine and co-workers into the freely available software package DDSCAT.[71] The DDA technique represents the cylindrical target by an array of N dipoles within a cubic grid (Figure S6, Supporting Information). It then calculates the polarizability, α_i, of each dipole based upon the dipole dielectric properties and position within the target r_i. After the dipole

polarizabilities have been calculated, it is then possible to calculate the target absorption C_{abs} and scattering C_{sca} cross sections as detailed below.[55,72−75]

If the index $i = 1, ... N$ represents each dipole within a cubic lattice then the instantaneous dipole moment, P_i is[72]

$$P_i = \alpha_i \times E_{loc,i} \quad (15)$$

where α_i is the dipole polarizability tensor and the electric field $E_{loc,i}$ is the sum of the incident electric field $E_{inc(r_i,t)}$ and the radiated electric field $E_{dip,i}$ from the surrounding $N - 1$ dipoles

$$E_{loc,i} = E_{inc(r_i,t)} + E_{dip,i} \quad (16)$$

with

$$E_{inc(r_i,t)} = E_o e^{i(kr_i - \omega t)} \quad (17)$$

where E_o is the amplitude of the electric field, k is the wavenumber, r_i is the position vector, ω is the angular frequency, and t is time.

Equation 18 represents the contribution to the incident electric field made by the radiated electric field from dipole j at position r_j within the $3x3$ matrix A_{ij}[73]

$$E_{dip,i} = \sum_{j \neq i} A_{ij} \times P_j \quad (18)$$

$$\therefore E_{loc,i} = E_o e^{i(kr_i - \omega t)} - \sum_{j \neq i} A_{ij} \times P_j \quad (19)$$

Each element A_{ij} is defined by the equation for an electric field from a radiating or oscillating dipole[72,73]

$$A_{ij} \cdot P_j = \frac{e^{ikr_{ij}}}{r_{ij}^3} \left\{ k^2 r_{ij} \times (r_{ij} \times P_j) + \frac{(1 - ikr_{ij})}{r_{ij}^2} [r_{ij}^2 P_j - 3r_{ij}(r_{ij} \times P_j)] \right\} \quad (20)$$

where $i \neq j$.

Substituting eq 19 into eq 15 and simplifying to find $E_{inc(r_i,t)}$ gives a set of $3N$ linear equations.[73]

$$E_{inc(r_i,t)} = \frac{P_i}{\alpha_i} + \sum_{j \neq i} A_{ij} \times P_j \quad (21)$$

The Parallel iterative methods (PIM)[71] package within DDSCAT uses iteration of the preconditioned biconjugate gradient with stabilization (PBCGST) algorithm to solve eq 21 for P_i. Once P_i is known, C_{abs} and C_{sca} can be calculated from eqs 22[72] and 23,[55] respectively.

$$C_{abs} = \frac{4\pi k}{|E_{inc}|^2} \sum_{i=1}^{N} \left\{ Im[P_i \times (\alpha_i^{-1})^* P_i^*] - \frac{2}{3} k^3 |P_i|^2 \right\} \quad (22)$$

$$C_{ext} = \frac{4\pi k}{|E_{inc}|^2} \sum_{i=1}^{N} Im(E_{inc,i}^* \times P_i) \quad (23)$$

The dielectric table of Frederikse and Weaver[58] for electropolished Au was used for the rod calculations, and the incident wavelength and the refractive index were divided by the refractive index of water (1.331) to get the relative refractive index. Orientation-averaged calculations were performed where the cylindrical rod target is initially assumed to have its long axis along the y-axis and its short axis along the x-axis. The incident wavevector k propagates along the x-axis and polarization is considered along both the y- and z-axes. The rod or target is assumed to have two unit vectors $\hat{\mathbf{a}}_1$ and $\hat{\mathbf{a}}_2$ to be fixed within the target; $\hat{\mathbf{a}}_1$ describes the longest axis of the rod, and $\hat{\mathbf{a}}_2$ must be orthogonal to $\hat{\mathbf{a}}_1$ and describes the shortest axis of the rod. The target was rotated 90° (in three incremental steps) through the angles of θ and ϕ, which specify the direction of $\hat{\mathbf{a}}_1$ with respect

to k, with the aim of calculating orientation-averaged extinction spectra.

To ensure the accuracy of the DDA technique, it is necessary to increase the number of dipoles to such a point where the results converge. The DDSCAT authors recommend that the interdipole spacing, d, be small compared to any structural lengths in the target and the wavelength λ of the incident light. The second criteria are satisfied with a high degree of accuracy if $|m|kd < 0.5$, where m is the refractive index of the target. The difficulty here is that as the number of dipoles within the target increases so does the computational time. So a compromise must be met between calculation accuracy and computational expense. Convergence was confirmed for the nanorod calculations presented here, and it was found that an interdipole spacing of either 1 or 2 nm (depending upon the size of the rod) was sufficient for convergence.

REFERENCES AND NOTES

1. Link, S.; Mohamed, M. B.; El-Sayed, M. A. Simulation of the Optical Absorption Spectra of Gold Nanorods as a Function of Their Aspect Ratio and the Effect of the Medium Dielectric Constant. *J. Phys. Chem. B* **1999**, *103*, 3073–3077.

2. Jana, N. R.; Gearheart, L.; Murphy, C. J. Seed-Mediated Growth Approach for Shape-Controlled Synthesis of Spheroidal and Rod-like Gold Nanoparticles Using a Surfactant Template. *Adv. Mater.* **2001**, *13*, 1389–1393.

3. Jana, N. R.; Gearheart, L.; Murphy, C. J. Wet Chemical Synthesis of Silver Nanorods and Nanowires of Controllable Aspect Ratio. *Chem. Commun.* **2001**, 617–618.

4. Jana, N. R.; Gearheart, L.; Murphy, C. J. Wet Chemical Synthesis of High Aspect Ratio Cylindrical Gold Nanorods. *J. Phys. Chem. B* **2001**, *105*, 4065–4067.

5. Nikoobakht, B.; El-Sayed, M. A. Preparation and Growth Mechanism of Gold Nanorods (NRs) Using Seed-Mediated Growth Method. *Chem. Mater.* **2003**, *15*, 1957–1962.

6. Im, S. H.; Lee, Y. T.; Wiley, B.; Xia, Y. N. Large-Scale Synthesis of Silver Nanocubes: The Role of HCl in Promoting Cube Perfection and Monodispersity. *Angew. Chem., Int. Ed.* **2005**, *44*, 2154–2157.

7. Jin, R. C.; Cao, Y. W.; Mirkin, C. A.; Kelly, K. L.; Schatz, G. C.; Zheng, J. G. Photoinduced Conversion of Silver Nanospheres to Nanoprisms. *Science* **2001**, *294*, 1901–1903.

8. Jin, R. C.; Cao, Y. C.; Hao, E. C.; Metraux, G. S.; Schatz, G. C.; Mirkin, C. A. Controlling Anisotropic Nanoparticle Growth through Plasmon Excitation. *Nature* **2003**, *425*, 487–490.

9. Millstone, J. E.; Park, S.; Shuford, K. L.; Qin, L. D.; Schatz, G. C.; Mirkin, C. A. Observation of a Quadrupole Plasmon Mode for a Colloidal Solution of Gold Nanoprisms. *J. Am. Chem. Soc.* **2005**, *127*, 5312–5313.

10. Xue, C.; Mirkin, C. A. pH-Switchable Silver Nanoprism Growth Pathways. *Angew. Chem., Int. Ed.* **2007**, *46*, 2036–2038.

11. Wiley, B. J.; Xiong, Y.; Li, Z.-Y.; Yin, Y.; Xia, Y. Right Bipyramids of Silver: A New Shape Derived from Single Twinned Seeds. *Nano Lett.* **2006**, *6*, 765–768.

12. Zhang, J.; Li, S. Z.; Wu, J. S.; Schatz, G. C.; Mirkin, C. A. Plasmon-Mediated Synthesis of Silver Triangular Bipyramids. *Angew. Chem., Int. Ed.* **2009**, *48*, 7787–7791.

13. Chen, J. Y.; Wiley, B.; Li, Z. Y.; Campbell, D.; Saeki, F.; Cang,

H.; Au, L.; Lee, J.; Li, X. D.; Xia, Y. N. Gold Nanocages: Engineering Their Structure for Biomedical Applications. *Adv. Mater.* **2005**, *17*, 2255–2261.

14. Wang, Z. L. Transmission Electron Microscopy of Shape-Controlled Nanocrystals and Their Assemblies. *J. Phys. Chem. B* **2000**, *104*, 1153–1175.

15. Sau, T. K.; Murphy, C. J. Room Temperature, High-Yield Synthesis of Multiple Shapes of Gold Nanoparticles in Aqueous Solution. *J. Am. Chem. Soc.* **2004**, *126*, 8648–8649.

16. Niu, W. X.; Zheng, S. L.; Wang, D. W.; Liu, X. Q.; Li, H. J.; Han, S. A.; Chen, J.; Tang, Z. Y.; Xu, G. B. Selective Synthesis of Single-Crystalline Rhombic Dodecahedral, Octahedral, and Cubic Gold Nanocrystals. *J. Am. Chem. Soc.* **2009**, *131*, 697–703.

17. Yu, Y.; Zhang, Q.; Lu, X.; Lee, J. Y. Seed-Mediated Synthesis of Monodisperse Concave Trisoctahedral Gold Nanocrystals with Controllable Sizes. *J. Phys. Chem. C* **2010**, *114*, 11119–11126.

18. Kelly, K. L.; Coronado, E.; Zhao, L. L.; Schatz, G. C. The Optical Properties of Metal Nanoparticles: The Influence of Size, Shape, and Dielectric Environment. *J. Phys. Chem. B* **2003**, *107*, 668–677.

19. Xue, C.; Millstone, J. E.; Li, S. Y.; Mirkin, C. A. Plasmon-Driven Synthesis of Triangular Core−Shell Nanoprisms from Gold Seeds. *Angew. Chem., Int. Ed.* **2007**, *46*, 8436–8439.

20. Sonnichsen, C.; Alivisatos, A. P. Gold Nanorods as Novel Nonbleaching Plasmon-Based Orientation Sensors for Polarized Single-Particle Microscopy. *Nano Lett.* **2005**, *5*, 301–304.

21. Mirkin, C. A.; Letsinger, R. L.; Mucic, R. C.; Storhoff, J. J. A DNA-Based Method for Rationally Assembling Nanoparticles into Macroscopic Materials. *Nature* **1996**, *382*, 607–609.

22. Elghanian, R.; Storhoff, J. J.; Mucic, R. C.; Letsinger, R. L.; Mirkin, C. A. Selective Colorimetric Detection of Polynucleotides Based on the Distance-Dependent Optical Properties of Gold Nanoparticles. *Science* **1997**, *277*, 1078–1081.

23. Sonnichsen, C.; Reinhard, B. M.; Liphardt, J.; Alivisatos, A. P. A Molecular Ruler Based on Plasmon Coupling of Single Gold and Silver Nanoparticles. *Nat. Biotechnol.* **2005**, *23*, 741–745.

24. Haes, A. J.; Van Duyne, R. P. A Nanoscale Optical Biosensor: Sensitivity and Selectivity of an Approach Based on the Localized Surface Plasmon Resonance Spectroscopy of Triangular Silver Nanoparticles. *J. Am. Chem. Soc.* **2002**, *124*, 10596–10604.

25. Possin, G. E. A Method for Forming Very Small Diameter Wires. *Rev. Sci. Instrum.* **1970**, *41*, 772–774.

26. Preston, C. K.; Moskovits, M. Optical Characterization of Anodic Aluminum-Oxide Films Containing Electrochemically Deposited Metal Particles. 1. Gold in Phosphoric-Acid Anodic Aluminum-Oxide Films. *J. Phys. Chem.* **1993**, *97*, 8495–8503.

27. Martin, C. R. Nanomaterials: A Membrane-Based Synthetic Approach. *Science* **1994**, *266*, 1961–1966.

28. Almawlawi, D.; Liu, C. Z.; Moskovits, M. Nanowires Formed in Anodic Oxide Nanotemplates. *J. Mater. Res.* **1994**, *9*, 1014–1018.

29. Wagner, R. S.; Ellis, W. C. Vapor−Liquid−Solid Mechanism of Single Crystal Growth. *Appl. Phys. Lett.* **1964**, *4*, 89–90.

30. Hurst, S.; Payne, E.; Qin, L.; Mirkin, C. A. Multisegmented One-Dimensional Nanorods Prepared by Hard-Template Synthetic Methods. *Angew. Chem., Int. Ed.* **2006**, *45*, 2672–2692.

31. Jorritsma, J.; Gijs, M. A. M.; Kerkhof, J. M.; Stienen, J. G. H. General Technique for Fabricating Large Arrays of Nanowires. *Nanotechnology* **1996**, *7*, 263–265.

32. Park, H.; Lim, A. K. L.; Alivisatos, A. P.; Park, J.; McEuen, P. L. Fabrication of Metallic Electrodes with Nanometer Separation by Electromigration. *Appl. Phys. Lett.* **1999**, *75*, 301–303.

33. Zheng, G.; Qin, L.; Mirkin, C. Spectroscopically Enhancing Electrical Nanotraps. *Angew. Chem., Int. Ed.* **2008**, *47*, 1938–1941.

34. Zheng, G.; Chen, X.; Mirkin, C. A. Complementary Electrical and Spectroscopic Detection Assays with On-Wire-Lithography-Based Nanostructures. *Small* **2009**, *5*, 2537–2540.

35. Huang, X.; El-Sayed, I. H.; Qian, W.; El-Sayed, M. A. Cancer Cell Imaging and Photothermal Therapy in the Near-Infrared Region by Using Gold Nanorods. *J. Am. Chem. Soc.* **2006**, *128*, 2115–2120.

36. Payne, E. K.; Shuford, K. L.; Park, S.; Schatz, G. C.; Mirkin, C. A. Multipole Plasmon Resonances in Gold Nanorods. *J. Phys. Chem. B* **2006**, *110*, 2150–2154.

37. Qin, L. D.; Zou, S. L.; Xue, C.; Atkinson, A.; Schatz, G. C.; Mirkin, C. A. Designing, Fabricating, and Imaging Raman Hot Spots. *Proc. Natl. Acad. Sci. U.S.A.* **2006**, *103*, 13300–13303.

38. Qin, L.; Banholzer, M. J.; Xu, X.; Huang, L.; Mirkin, C. A., Rational Design and Synthesis of Catalytically Driven Nanorotors. *J. Am. Chem. Soc.* **2007**, *129*, 14870−14871.

39. Wei, W.; Li, S. Z.; Qin, L. D.; Xue, C.; Millstone, J. E.; Xu, X. Y.; Schatz, G. C.; Mirkin, C. A. Surface Plasmon-Mediated Energy Transfer in Heterogap Au−Ag Nanowires. *Nano Lett.* **2008**, *8*, 3446–3449.

40. Slaughter, L. S.; Chang, W.-S.; Swanglap, P.; Tcherniak, A.; Khanal, B. P.; Zubarev, E. R.; Link, S. Single-Particle Spectroscopy of Gold Nanorods Beyond the Quasi-Static Limit: Varying the Width at Constant Aspect Ratio. *J. Phys. Chem. C* **2010**, *114*, 4934–4938.

41. Alekseeva, A. V.; Bogatyrev, V. A.; Khlebtsov, B. N.; Mel'nikov, A. G.; Dykman, L. A.; Khlebtsov, N. G. Gold Nanorods: Synthesis and Optical Properties. *Colloid J.* **2006**, *68*, 661–678.

42. Perez-Juste, J.; Pastoriza-Santos, I.; Liz-Marzan, L. M.; Mulvaney, P. Gold Nanorods: Synthesis, Characterization and Applications. *Coord. Chem. Rev.* **2005**, *249*, 1870–1901.

43. Myroshnychenko, V.; Rodriguez-Fernandez, J.; Pastoriza-Santos, I.; Funston, A. M.; Novo, C.; Mulvaney, P.; Liz-Marzan, L. M.; de Abajo, F. J. G. Modelling the Optical Response of Gold Nanoparticles. *Chem. Soc. Rev.* **2008**, *37*, 1792–1805.

44. Huang, X. H.; Neretina, S.; El-Sayed, M. A. Gold Nanorods: From Synthesis and Properties to Biological and Biomedical Applications. *Adv. Mater.* **2009**, *21*, 4880–4910.

45. Novo, C.; Gomez, D.; Perez-Juste, J.; Zhang, Z. Y.; Petrova, H.; Reismann, M.; Mulvaney, P.; Hartland, G. V. Contributions from Radiation Damping and Surface Scattering to the Linewidth of the Longitudinal Plasmon Band of Gold Nanorods: A Single Particle Study. *Phys. Chem. Chem. Phys.* **2006**, *8*, 3540–3546.

46. Foss, C. A.; Hornyak, G. L.; Stockert, J. A.; Martin, C. R. Template-Synthesized Nanoscopic Gold Particles—Optical-Spectra and the Effects of Particle-Size and Shape. *J. Phys. Chem.* **1994**, *98*, 2963–2971.

47. Gans, R. Über Die Form Ultramikroskopischer Goldteilchen. *Ann. Phys.* **1912**, *342*, 881–900.

48. Encina, E. R.; Coronado, E. A. Resonance Conditions for Multiple Plasmon Excitations in Noble Metal Nanorods. *J. Phys. Chem. C* **2007**, *111*, 16796–16801.

49. Sonnichsen, C.; Franzl, T.; Wilk, T.; von Plessen, G.; Feldmann, J.; Wilson, O.; Mulvaney, P. Drastic Reduction of Plasmon Damping in Gold Nanorods. *Phys. Rev. Lett.* **2002**, *88*, 077402.

50. Prescott, S. W.; Mulvaney, P. Gold Nanorod Extinction Spectra. *J. Appl. Phys.* **2006**, *99*, 123504.

51. Qin, L.; Park, S.; Huang, L.; Mirkin, C. A. On-Wire Lithography. *Science* **2005**, *309*, 113–115.

52. Qin, L. D.; Jang, J. W.; Huang, L.; Mirkin, C. A. Sub-5-nm Gaps Prepared by On-Wire Lithography: Correlating Gap Size with Electrical Transport. *Small* **2007**, *3*, 86–90.

53. Elnathan, R.; Kantaev, R.; Patolsky, F. Synthesis of Hybrid Multicomponent Disklike Nanoparticles. *Nano Lett.* **2008**, *8*, 3964–3972.

ARTICLE

54. Masuda, H.; Fukuda, K. Ordered Metal Nanohole Arrays Made by a Two-Step Replication of Honeycomb Structures of Anodic Alumina. *Science* **1995**, *268*, 1466–1468.

55. Draine, B. T. The Discrete-Dipole Approximation and Its Application to Interstellar Graphite Grains. *J. Astrophys.* **1988**, *333*, 848–872.

56. Draine, B. T.; Flatau, P. J. Discrete-Dipole Approximation for Scattering Calculations. *J. Opt. Soc. Am. A* **1994**, *11*, 1491–1499.

57. Purcell, E. M.; Pennypacker, C. R. Scattering and Absorption of Light by Nonspherical Dielectric Grains. *J. Astrophys.* **1973**, *186*, 705.

58. Weaver, J. H.; Frederikse, H. P. R. *Optical Properties of Selected Elements*; 82nd ed.; CRC Press: Boca Raton, FL, 2001; p 12.

59. Harris, N.; Ford, M. J.; Mulvaney, P.; Cortie, M. B. Tunable Infrared Absorption by Meta Nanoparticles: The Case for Gold Rods and Shells. *Gold Bull.* **2008**, *41*, 5–14.

60. Khlebstov, B. N.; Khlebstov, N. G. Multipole Plasmons in Metal Nanorods: Scaling Properties and Dependence on Particle Size, Shape, Orientation, and Dielectric Environment. *J. Phys. Chem. C* **2007**, *111*, 11516–11527.

61. Bryant, G. W.; de Abajo, F. J. G.; Aizpurua, J. Mapping the Plasmon Resonances of Metallic Nanoantennas. *Nano Lett.* **2008**, *8*, 631–636.

62. Meier, M.; Wokaun, A. Enhanced Fields on Large Metal Particles: Dynamic Depolarization. *Opt. Lett.* **1983**, 581–583.

63. Zeman, E. J.; Schatz, G. C. An Accurate Electromagnetic Theory Study of Surface Enhancement Factors for Ag, Au, Cu, Li, Na, Al, Ga, in, Zn, and Cd. *J. Phys. Chem.* **1987**, *91*, 634–643.

64. Bohren, C. F.; Huffman, D. R. *Absorption and Scattering of Light by Small Particles*; Wiley: Weinheim, Germany, 2004.

65. Moroz, A. Depolarization Field of Spheroidal Particles. *J. Opt. Soc. Am. B* **2009**, *26*, 517–527.

66. Palik, E. D. *Handbook of Optical Constants of Solids*; Academic Press: New York, 1985.

67. Arnold, M. D.; Blaber, M. G. Optical Performance and Metallic Absorption in Nanoplasmonic Systems. *Opt. Express* **2009**, *17*, 3835–3847.

68. Wang, F.; Shen, Y. R. General Properties of Local Plasmons in Metal Nanostructures. *Phys. Rev. Lett.* **2006**, *97*, 206806.

69. Banholzer, M. J.; Qin, L. D.; Millstone, J. E.; Osberg, K. D.; Mirkin, C. A. On-Wire Lithography: Synthesis, Encoding and Biological Applications. *Nat. Protoc.* **2009**, *4*, 838–848.

70. Okamoto, F. Chemical Etchants for Fabrication of Thin-Film Patterns of Silver on Acid-Sensitive and Base-Sensitive Oxides. *Jpn. J. Appl. Phys.* **1974**, *13*, 383–384.

71. Draine, B. T.; Flatau, P. J. User Guide for the Discrete Dipole Approximation Code Ddscat 6.1,http://arxiv.org/abs/astro-ph/0409262, 2004.

72. Brioude, A.; Jiang, X. C.; Pileni, M. P. Optical Properties of Gold Nanorods: DDA Simulations Supported by Experiments. *J. Phys. Chem. B* **2005**, *109*, 13138–13142.

73. Goodman, J. J.; Draine, B. T.; Flatau, P. J. Application of Fast-Fourier-Transform Techniques to the Discrete-Dipole Approximation. *Opt. Lett.* **1991**, *16*, 1198–1200.

74. Collinge, M. J.; Draine, B. T. Discrete-Dipole Approximation with Polarizabilities That Account for Both Finite Wavelength and Target Geometry. *J. Opt. Soc. Am. A* **2004**, *21*, 2023–2028.

75. Felidj, N.; Aubard, J.; Levi, G. Discrete Dipole Approximation for Ultraviolet−Visible Extinction Spectra Simulation of Silver and Gold Colloids. *J. Chem. Phys.* **1999**, *111*, 1195–1208.